The Astrophysical Journal, 956:97 (8pp), 2023 October 20 https://doi.org/10.3847/1538-4357/acf846

XMM-Newton and INTEGRAL Observations of the Bright GRB 230307A: Vanishing of the Local Absorption and Limits on the Dust in the Magellanic Bridge

Sandro Mereghetti[1], Michela Rigoselli[1], Ruben Salvaterra[1], Andrea Tiengo[1,2], and Dominik P. Pacholski[1,3]
[1] Istituto Nazionale di Astrofisica, Istituto di Astrofisica Spaziale e Fisica Cosmica di Milano, via A. Corti 12, I-20133 Milano, Italy; sandro.mereghetti@inaf.it
[2] Scuola Universitaria Superiore IUSS Pavia, Piazza della Vittoria 15, I-27100 Pavia, Italy
[3] Dipartimento di Fisica G. Occhialini, Università degli Studi di Milano Bicocca, Piazza della Scienza 3, I-20126 Milano, Italy
Received 2023 July 30; revised 2023 August 30; accepted 2023 September 9; published 2023 October 12

Abstract

GRB 230307A is the second brightest gamma-ray burst detected in more than 50 years of observations and is located in the direction of the Magellanic Bridge. Despite its long duration, it is most likely the result of the merger of a compact binary ejected from a galaxy in the local universe (redshift $z = 0.065$). Our XMM-Newton observation of its afterglow at 4.5 days shows a power-law spectrum with photon index $\Gamma = 1.73 \pm 0.10$, unabsorbed flux $F_{0.3-10\ \mathrm{keV}} = (8.8 \pm 0.5) \times 10^{-14}$ erg cm^{-2} s^{-1}, and no absorption in excess of that produced in our Galaxy and in the Magellanic Bridge. We derive a limit of $N_{\mathrm{H}}^{\mathrm{HOST}} < 5 \times 10^{20}$ cm^{-2} on the absorption at the GRB redshift, which is a factor ∼5 below the value measured during the prompt phase. We searched for the presence of dust scattering rings with negative results and set an upper limit of the order of $A_V < 0.05$ on the absorption from dust in the Magellanic Bridge.

Unified Astronomy Thesaurus concepts: Gamma-ray bursts (629); Interstellar dust (836); Magellanic Clouds (990)

1. Introduction

Not many years after their discovery, it was recognized that gamma-ray bursts (GRBs) can be divided into two groups, based mostly on their duration and, to a lesser extent, spectral hardness (Norris et al. 1984; Kouveliotou et al. 1993). It was later realized that this phenomenological distinction is related to different formation mechanisms. GRBs of the "long" class have been firmly associated with Type Ib/c core-collapse supernovae of massive stars (e.g., Galama et al. 1998; Hjorth et al. 2003; Stanek et al. 2003). The progenitors of the "short" GRBs remained elusive for a longer time, even though many hints consistently pointed to a compact binary merger progenitor (e.g., Narayan et al. 1992; Mochkovitch et al. 1993; Nakar 2007). This was finally confirmed by the association of the short GRB 170817A with the gravitational-wave signal GW 170817 produced by a binary neutron star merger (Abbott et al. 2017a, 2017b; Goldstein et al. 2017; Savchenko et al. 2017b).

However, several results obtained in the last few years indicate that a classification based only on duration does not always reflect the intrinsic properties related to the GRB origin. For example, the short GRB 090426 resembled long bursts as far as its spectrum, energetics, and afterglow properties are concerned (Antonelli et al. 2009; Nicuesa Guelbenzu et al. 2011). Evidence for a supernova, as usually detected in nearby collapsar-like events, was found for GRB 040924 and GRB 200826A (Wiersema et al. 2008; Ahumada et al. 2021; Rossi et al. 2022), which, although not extremely short, had rest-frame durations below 2 s. On the other hand, deep observations of some long GRBs at low redshift failed to detect supernovae down to stringent limits (Fynbo et al. 2006), while kilonova signatures calling for an origin in a compact object merger have been associated with bursts of long duration, such as GRB 060614 (Yang et al. 2015) and, more recently, GRB 211221A (Rastinejad et al. 2022; Troja et al. 2022; Yang et al. 2022). A classification in terms of Type I/II, respectively for mergers and collapsars, thus seems more convenient (Zhang 2006).

A recent example of a GRB with long duration (∼150 s) but most likely originating from a compact binary merger is provided by GRB 230307A (Levan et al. 2023a; Dichiara et al. 2023; Sun et al. 2023; Wang et al. 2023). The evidence for a Type I classification comes from the James Webb Space Telescope discovery of an associated kilonova (Levan et al. 2023a; Yang et al. 2023), similar to that seen for the gravitational-wave merger GW 170817 (Abbott et al. 2017a). Most likely, the binary merger was ejected from a galaxy seen at an angular offset of 30″ from GRB 230307A. Given the galaxy's redshift of $z = 0.065$, this corresponds to a large, but still plausible, projected distance of about 40 kpc. The alternative association with a galaxy at redshift $z = 3.87$ (Levan et al. 2023b) is unlikely because it would imply an unprecedented isotropic energy as large as 10^{56} erg and, at such a high redshift, the observed rapidly varying kilonova-like emission corresponds to rest-frame rise and decay times too short for a supernova of this luminosity. Furthermore, the spectroscopic detection of an emission line at 2.15 μm, interpreted as due to tellurium, makes the low-redshift Type I GRB hypothesis very strong (Levan et al. 2023a)

GRB 230307A immediately attracted much interest owing to its very large fluence of a few 10^{-3} erg cm^{-2} (Dalessi & Fermi GBM Team 2023; Dalessi et al. 2023), surpassed only by that of the exceptional GRB 221009A[4] (Xiong et al. 2023; Burns et al. 2023a; Svinkin et al. 2023). GRB 230307A is also interesting because it occurred in the direction of the Magellanic Bridge, a structure consisting mainly of H I, which

[4] Although the occurrence within six months of each other of the two brightest GRBs ever observed seems at first remarkable, the time distribution of the complete sample of 17 GRBs with fluence above 10^{-3} erg cm^{-2} detected since 1971 (Table 2 of Burns et al. 2023b) is fully consistent with a constant rate.

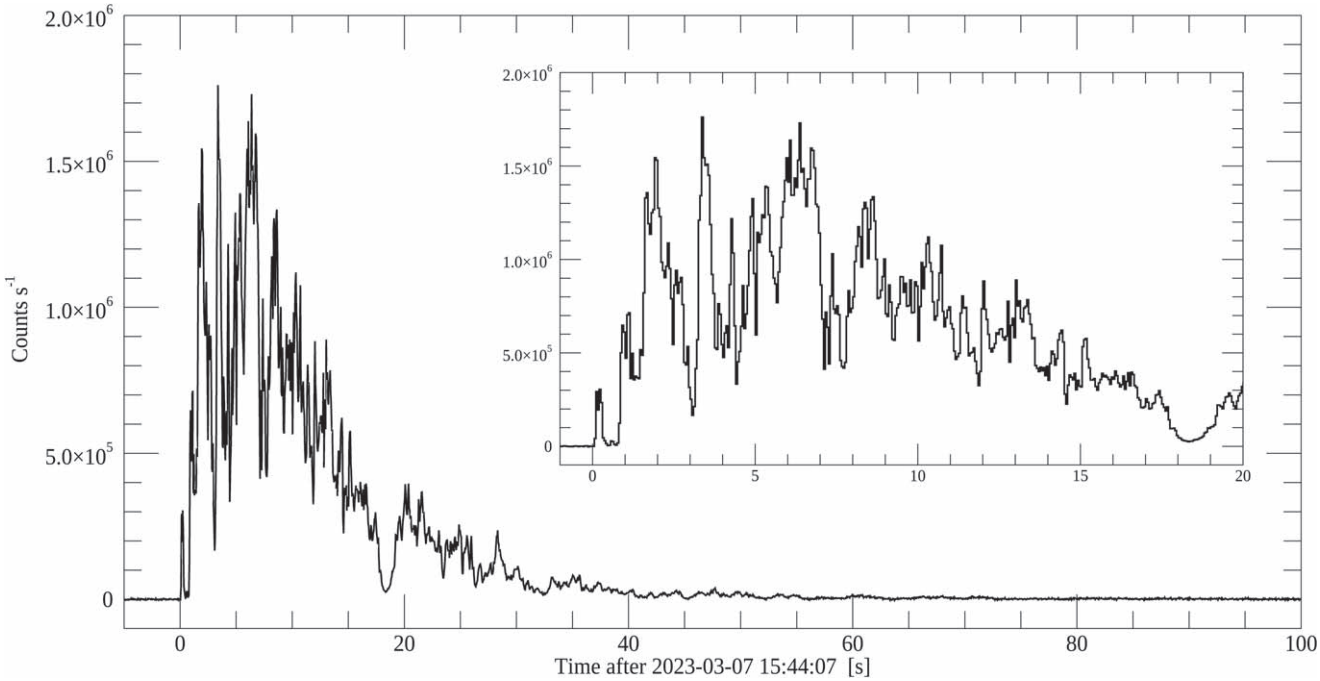

Figure 1. Light curve of GRB 230307A at energies above 75 keV obtained with the SPI/ACS detector. The bin size is 50 ms. The inset shows a zoom of the initial part.

connects the Small and Large Magellanic Clouds and was probably produced by the tidal interaction between these two galaxies (see, e.g., Gaia Collaboration et al. 2021, and references therein). The occurrence of a bright GRB in this direction offers the possibility to constrain the poorly known properties of the interstellar dust in the Bridge through the analysis of scattered X-ray radiation, as done for Galactic dust clouds with other GRBs (Vaughan et al. 2004, 2006; Tiengo & Mereghetti 2006; Vianello et al. 2007; Pintore et al. 2017; Tiengo et al. 2023).

Here we report the results of an XMM-Newton observation of GRB 230307A carried out about 5 days after the burst occurred (Section 2.2), complemented by data of the prompt emission in the hard X-ray range obtained with the INTEGRAL satellite (Section 2.1). In Section 2.3 we use the X-ray data to look for the presence of dust scattering rings and to derive constraints on the amount of dust in the Magellanic Bridge.

2. Data Analysis and Results

2.1. Prompt Gamma-Ray Emission with INTEGRAL

GRB 230307A was detected by the Anti-Coincidence Shield (ACS) of the SPI instrument on board the INTEGRAL satellite. The ACS, besides serving as an active shield for the germanium detectors of SPI, acts as a nearly omnidirectional detector with high sensitivity at energies above ∼75 keV (von Kienlin et al. 2003). It provides data with fixed time resolution of 50 ms in a single energy channel and without directional information. The burst occurred at an angle of 75° with respect to the INTEGRAL pointing direction, and at an azimuthal angle for which the ACS is not obstructed by other instruments on board the satellite. Therefore, the ACS provided an optimal response for the direction of GRB 230307A (see, e.g., Savchenko et al. 2017a).

The ACS light curve of GRB 230307A is presented in Figure 1. The burst showed remarkable variability on short timescales, within an envelope with a fast rise and a slower decay. The T_{90} duration is 28.6 s, but significant emission is visible up to 130 s after $T_0 = 15{:}44{:}07$ UT. The burst starts with a ∼0.2 s long precursor, which contains ∼0.4% of the total fluence. This is followed by a multipeaked pulse lasting about 17 s, until a dip at about $T_0 + 18$ s. The temporal decay after $T_0 + 20$ s can be approximated by a power law with index $\alpha = -3.467 \pm 0.007$. The total fluence, from T_0 to $T_0 + 130$ s, is $(1.5239 \pm 0.0008) \times 10^7$ ACS counts, which, adopting the average conversion factor of 1 ACS count $\sim 10^{-10}$ erg cm^{-2} (Viganò & Mereghetti 2009), corresponds to $\sim 1.52 \times 10^{-3}$ erg cm^{-2} in the 75–1000 keV range.

2.2. X-Ray Afterglow with XMM-Newton

A 50 ks long Target of Opportunity observation of GRB 230307A was carried out with the XMM-Newton satellite, starting on 2023 March 12 at 02:16:54 UT, about 4.5 days after the GRB trigger. The EPIC-pn (Strüder et al. 2001) and the two EPIC-MOS (Turner et al. 2001) cameras were operated in full window mode, with the thin optical-blocking filter. After processing the data with the `SAS 19.1.3` (Gabriel et al. 2004) and the most recent calibration files, we selected the EPIC events with standard filtering expressions and removed time intervals of high background. This resulted in net exposure times of 37.2 ks (pn) and 41.5 ks (MOS). In addition to the GRB afterglow, several sources were detected (see the Appendix).

The afterglow spectra were extracted from a circular region of 30″ radius, centered at coordinates R.A. = $04^{\rm h}03^{\rm m}26^{\rm s}.24$, decl. = $-75°22'43''.8$, and those of the background from a nearby circle of 40″ radius. The spectra of the three cameras were rebinned with a minimum of 30 counts per bin and then fitted simultaneously using the XSPEC software (version

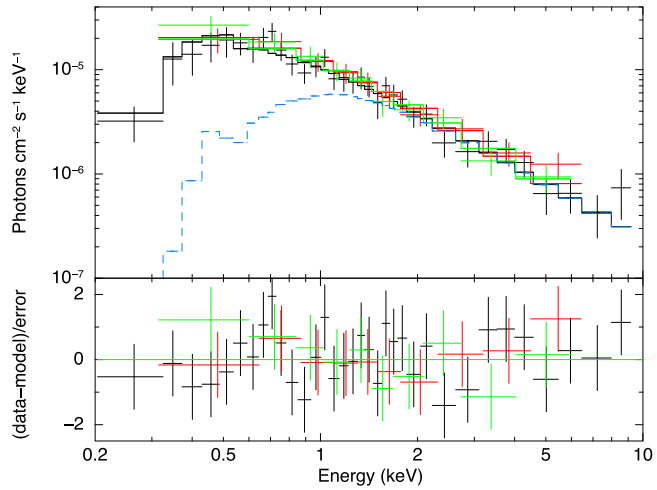

Figure 2. Top panel: EPIC-pn (black), -MOS1 (red), and -MOS2 (green) spectra of the afterglow of GRB 230307A fitted with an absorbed power law. The blue dashed line indicates, for comparison, the spectrum expected with the intrinsic absorption $N_{\rm H}^{\rm HOST} = 2.73 \times 10^{21}$ cm^{-2} measured in the prompt emission. Bottom panel: residuals of the best fit in units of σ.

12.13.0c). For the absorption model we used cross sections and abundances from Wilms et al. (2000). Errors on the spectral parameters are given at 1σ confidence level.

The spectra are well described (χ^2/dof = 29.14/49, null hypothesis probability (nhp) = 0.99) by an absorbed power law with photon index $\Gamma = 1.73 \pm 0.10$, column density $N_{\rm H} = (9 \pm 2) \times 10^{20}$ cm^{-2}, and unabsorbed flux $F_{0.3-10\ \rm keV} = (8.8 \pm 0.5) \times 10^{-14}$ erg cm^{-2} s^{-1} (see Figure 2).

The derived absorption is consistent with the local (Galactic plus Magellanic Clouds) column density in this direction, $N_{\rm H}^{\rm LOC} = 9.4 \times 10^{20}$ cm^{-2} (HI4PI Collaboration et al. 2016). Therefore, in order to constrain possible absorption in the GRB host, we fixed the column density to $N_{\rm H}^{\rm LOC}$ and added to the model a redshifted absorption component ($N_{\rm H}^{\rm HOST}$). We found that, at the GRB redshift $z = 0.065$, the host absorption is $N_{\rm H}^{\rm HOST} < 5 \times 10^{20}$ cm^{-2} (2σ upper limit, see Figure 3).

2.3. Limits on Dust in the Magellanic Bridge

We searched for the presence of dust-scattered events using the method based on "pseudo-distances" (Tiengo & Mereghetti 2006), which provides a higher sensitivity for expanding rings than a simple analysis of time-integrated images. Briefly, this method exploits the fact that for a source at a distance much greater than that of the dust, X-ray photons detected at an angle Θ from the source direction arrive with a time delay $t = (D/2c)\Theta^2$, where D is the distance of the dust. A pseudo-distance D_i can be computed for each detected count, based on its coordinates (x_i, y_i) and arrival time t_i:

$$D_i = \frac{2c(t_i - t_{\rm B})}{(x_i - x_{\rm B})^2 + (y_i - y_{\rm B})^2} \qquad (1)$$

where $x_{\rm B}$, $y_{\rm B}$, and $t_{\rm B}$ are the coordinates and time of the GRB. An expanding X-ray ring produced by dust at distance D appears as a Lorentzian peak in the D_i distribution.

To derive the D_i distribution we selected the XMM-Newton/EPIC events with energy in the range 0.5–4 keV, FLAG = 0, PATTERN $\leqslant$ 4 (pn) and $\leqslant$ 12 (MOS), and we removed several point sources (see the Appendix) by excluding circular regions of radius $\sim$20″. The resulting empty regions, as well as the

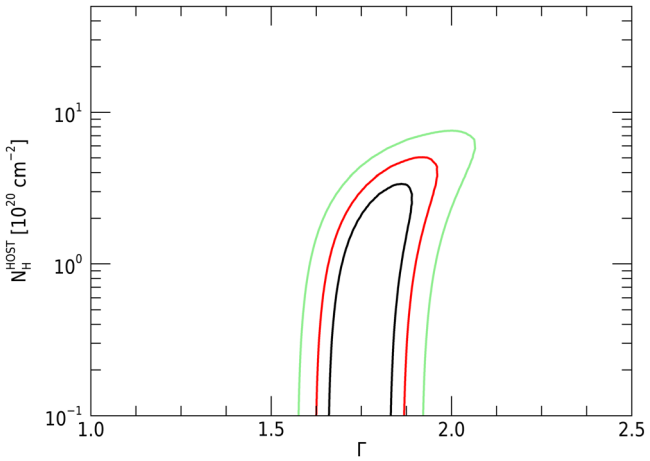

Figure 3. Confidence contours (1σ, 2σ, and 3σ) of photon index Γ and absorption at the GRB redshift $N_{\rm H}^{\rm HOST}$.

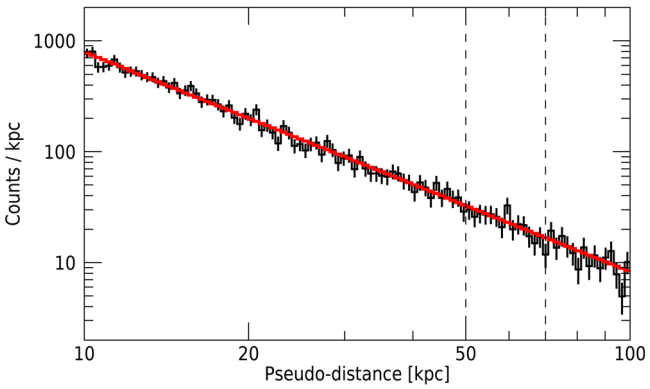

Figure 4. Pseudo-distance distribution extracted from EPIC-pn and -MOS events in the 0.5–4 keV energy range. The red line represents the best power-law fit to the data, while the vertical dashed lines indicate the relevant distance range for the analysis of interstellar dust in the Magellanic Bridge.

dead areas between CCD gaps, were filled with uniformly distributed events, in order to avoid artifacts and spurious peaks in the D_i distribution.

Most of the Galactic dust in this direction is concentrated in two layers at distances of 225 pc and 375 pc (Lallement et al. 2022), but, at the time of our observation, possible scattering rings produced by these layers had already expanded to angular radii of $\sim$19′ and $\sim$14.′5, outside the EPIC field of view. On the other hand, X-rays scattered by dust in the Magellanic Bridge can be detected because radii in the range $\sim$1′–2′ are expected in this case (see Figure 7).

As can be seen in Figure 4, the distribution of the D_i values does not show any prominent peak in the range of relevant distances. In fact it is well fit by a single power law with slope -1.98 ± 0.02 (χ^2/dof = 1.05, nhp = 0.35), as expected for uniformly distributed background counts and unscattered X-ray photons.

To derive upper limits on the scattered X-ray flux we carried out Monte Carlo simulations in which we added to the observed D_i histogram N_s photons distributed according to Lorentzian profiles expected for different distances of the dust. In principle, the Lorentzian width Γ depends on the thickness δD of the dust layer, but, in the case at hand, it is dominated by the finite angular resolution of the instrument ($\delta\Theta_{\rm FWHM} \sim 5''$), which results in $\Gamma = 2D\,|\delta\Theta_{\rm FWHM}/\Theta|$. At the mean time of the

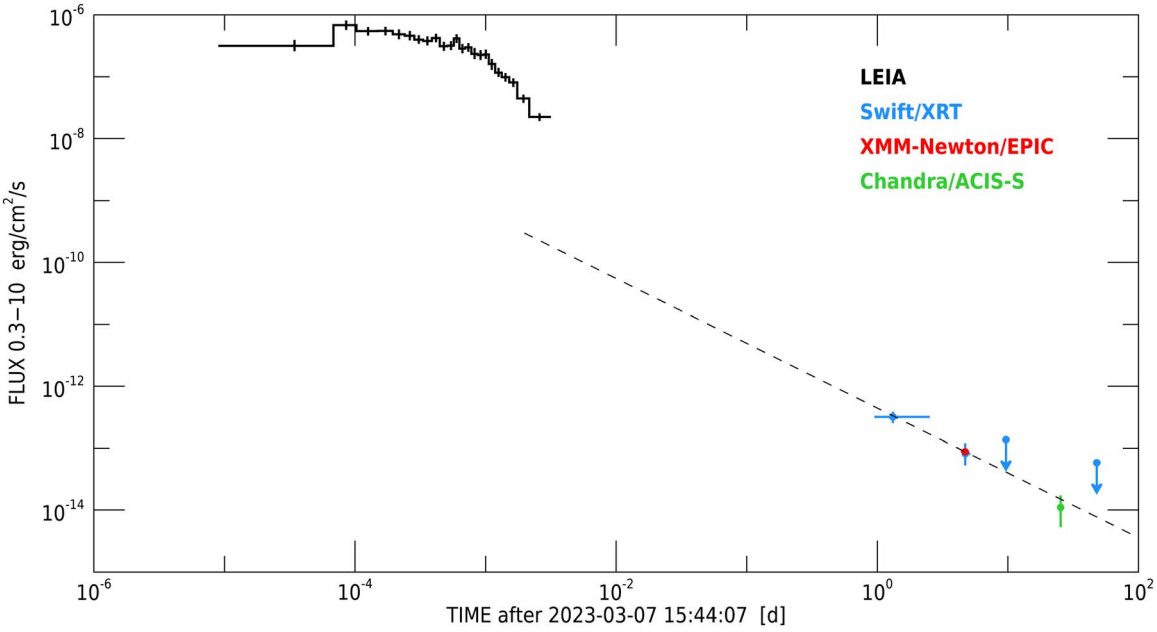

Figure 5. X-ray flux between 0.3 and 10 keV of GRB 230307A (black histogram: LEIA) and its afterglow (blue: Swift/XRT; red: XMM-Newton/EPIC; green: Chandra/ACIS-S). The light curve of the afterglow has been fitted with a power law in the range $T_0 + [1.3, 25.3]$ days (dashed line).

observation (4.7 days after the burst) this gives the value $\Gamma \sim 0.017 D_{\rm kpc}^{3/2}$ kpc, which we used in our simulations. These were carried out for two representative values, 50 and 70 kpc, which bracket possible distances for dust structures in the Magellanic Bridge (see, e.g., Jacyszyn-Dobrzeniecka et al. 2016). We found upper limits at the 95% confidence level of $N_s = 245$ EPIC counts for $D = 50$ kpc ($\Gamma = 6$ kpc) and $N_s = 260$ EPIC counts for $D = 70$ kpc ($\Gamma = 10$ kpc).

3. Discussion

The X-ray flux (0.3–10 keV) of our XMM-Newton observation is plotted in Figure 5, together with those from other available measurements of the X-ray afterglow. These are the Swift/XRT observations carried out at $T_0 + 1.3$ days (Burrows et al. 2023)[5] and $T_0 + 4.7$ days, and the Chandra observation at $T_0 + 25.3$ days (Rouco Escorial et al. 2023). We also show in Figure 5 the X-ray light curve of the prompt emission measured with LEIA in the 0.5–4 keV range (Sun et al. 2023), opportunely rescaled in the 0.3–10 keV range according to their spectrum (see below). The temporal evolution of the afterglow is well fitted by a power law of index $\alpha = -1.05 \pm 0.13$ and normalization $n = (4.4 \pm 0.9) \times 10^{-13}$ erg cm^{-2} s^{-1} at $T_0 + 1$ day.

The upper limit we derived at $T_0 + 4.5$ days on the host absorption, $N_{\rm H}^{\rm HOST} < 5 \times 10^{20}$ cm^{-2}, is significantly smaller than the value observed during the prompt emission phase, $N_{\rm H}^{\rm PROMPT} = 2.73 \times 10^{21}$ cm^{-2} (Sun et al. 2023). Evidence of variations in X-ray column density has been reported so far only for a handful of GRBs (Starling et al. 2005; Campana et al. 2007, 2021; Grupe et al. 2007). Indeed, a systematic analysis of 199 GRBs showed that only seven bursts display signs of a decrease in the intrinsic $N_{\rm H}$ (Valan et al. 2023), although the observed variation could also be explained in terms of spectral evolution of the afterglow emission. Variations in the X-ray absorption are predicted due to the ionization of the surrounding medium by the GRB radiation (Perna & Loeb 1998; Lazzati & Perna 2002; Perna & Lazzati 2002). However, it is unlikely that this scenario applies to the case at hand: at more than 40 kpc from its host galaxy, GRB 230307A probably exploded in a low-density environment, as also suggested by the relative faintness of its afterglow (Levan et al. 2023a; Yang et al. 2023). The absorption measured with LEIA during the prompt phase was most likely caused by very local material, possibly ejected during the last phases preceding the merger. The ejecta responsible for the absorption might have moved out of the line of sight by the time of the XMM-Newton observation. Another possibility is that the afterglow was produced at a large distance, not affected by material close to the central engine. A fully self-consistent model of mass ejection in short GRBs would be a significant step forward, but unfortunately this has not yet been developed. In this respect, more measurements of the X-ray absorption and its evolution during the initial phases of the burst would be very useful.

We searched for X-ray-scattering rings caused by dust in the Magellanic Bridge, with negative results. Assuming a model for the scattering cross section and knowing the X-ray fluence and spectrum of GRB 230307A, the upper limits on the number of scattered photons derived in Section 2.3 can be translated into limits on the amount of dust. We adopt the analytical dust model of Draine (2003) and the results obtained with the LEIA experiment (Sun et al. 2023) on the X-ray prompt emission (a power-law spectrum with photon index $\Gamma = 1.67$, $N_{\rm H}^{\rm LOC} = 9.41 \times 10^{20}$ cm^{-2}, $N_{\rm H}^{\rm HOST} = 2.73 \times 10^{21}$ cm^{-2}, and fluence $F_{0.5-4\,\rm keV} = 2.27 \times 10^{-5}$ erg cm^{-2}). The resulting limits of $A_V < 0.040$–0.056, for dust at distances in the 50–70 kpc range, show the potentiality of this method to constrain the dust properties in the Magellanic Bridge. However, we note that the results depend on the chosen dust model. As an example, adopting the BARE-GR-B model of Zubko et al. (2004), which provided the best fit in other observations of X-ray halos and rings produced by dust

[5] See also https://www.swift.ac.uk/xrt_products/TILED_GRB00110/Source2/curve and https://www.swift.ac.uk/xrt_curves/00021537/.

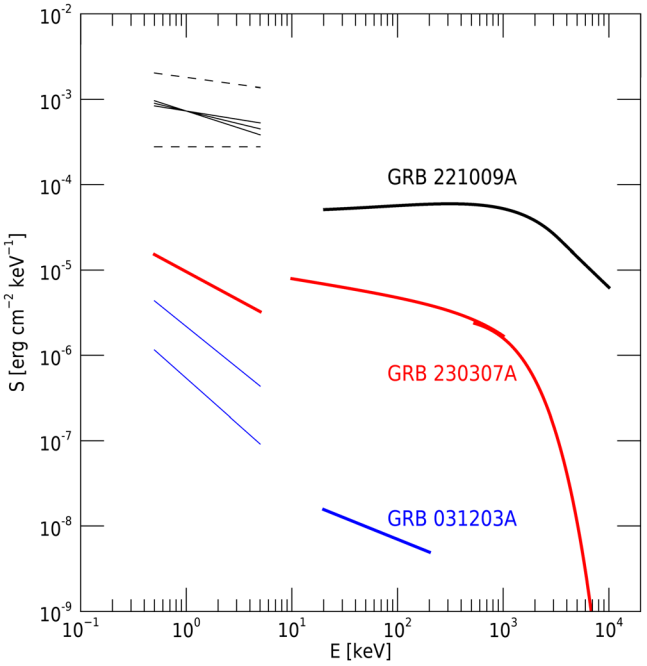

Figure 6. Broadband fluence spectra for three GRBs with detections or limits on the dust scattering. The spectra for GRB 230307A (red) are from Sun et al. (2023). For GRB 221009A (black) we indicate the best estimate (solid) and the maximum and minimum values (dashed) for the soft X-ray fluence derived from the analysis of dust scattering rings (Tiengo et al. 2023), while the gamma-ray spectrum is from Frederiks et al. (2023). For GRB 031203 (blue) we indicate two estimates of the soft X-ray fluence from dust scattering analysis by Tiengo & Mereghetti (2006) (lowest) and Watson et al. (2006) (highest), while the gamma-ray spectrum is from Vianello et al. (2009).

scattering (e.g., Smith et al. 2006; Tiengo et al. 2010, 2023), we can limit the quantity of dust in this part of the Magellanic Bridge to $A_V < 0.25$–0.32. Even so, these limits are more constraining than the total reddening $E(B-V) = 0.08 \pm 0.08$ reported in the map of Chen et al. (2022), which in this direction has a spatial resolution of 55′ and estimates the same reddening value also for foreground Galactic stars.

4. Conclusions

We have observed GRB 230307A with XMM-Newton in order to study its X-ray afterglow about five days after the burst and to search for dust scattering features, exploiting its very high brightness and fortuitous location close to the Large Magellanic Cloud.

The good counting statistics and wide energy range of the EPIC spectra allowed us to reveal a significant decrease in the absorption, which varied from 2.73×10^{21} cm^{-2} in the prompt emission phase to less than 5×10^{20} cm^{-2} during the afterglow at ∼4.5 days after the burst. This large variation suggests that the absorption in the prompt emission was caused by ejecta very close to the central engine, which moved out of the line of sight by the time of the XMM-Newton observation.

The study of dust-scattered X-rays from GRBs with sensitive telescopes offers great potentialities. As is schematically shown in Figure 6, in at least two cases, GRB 031203A (Watson et al. 2006; Tiengo & Mereghetti 2006) and GRB 221009A (Tiengo et al. 2023), this analysis provided evidence for a bright soft X-ray excess that could not be observed directly. Conversely, the prompt soft X-ray emission of GRB 230307A was directly observed and we could exploit the resulting information to set limits on the amount of dust in the Magellanic Bridge. Although the limits are not very deep in this particular case, our results indicate that more constraining observations are within reach of the current instrumentation. For example, an earlier XMM-Newton observation of GRB 230307A, performed when the X-rays potentially scattered by nearby dust clouds were still within the telescope field of view, would have allowed us to disentangle the effects of dust in our Galaxy from that of dust in the Magellanic Bridge.

Acknowledgments

The scientific results reported in this article are based on observations obtained with XMM-Newton and INTEGRAL, ESA science missions with instruments and contributions directly funded by ESA Member States, NASA, and Russia. We acknowledge financial support from the Italian Ministry for University and Research, through grants 2017LJ39LM (UNIAM) and INAF Large Program for Fundamental Research 2022. We thank the XMM-Newton Mission Scientist N. Schartel for granting the ToO observation and an anonymous referee for his/her useful comments.

Facilities: XMM, INTEGRAL.

Software: SAS (v19.1.0; Gabriel et al. 2004), HEASoft package (v.6.31; Nasa High Energy Astrophysics Science Archive Research Center (Heasarc) 2014), Xspec (v12.13.0c; Arnaud 1996), xscat (v1.0.0; Smith et al. 2016), dustmaps (v1.0.4; Green 2018).

Appendix
X-Ray Sources in the GRB 230307A Field

We reduced and filtered the EPIC data using standard procedures as described in Section 2.2 and created pn+MOS images in three energy bands: 0.5–2 keV, 2–12 keV, and 0.5–12 keV. These images were used to perform source detection using the SAS tool *edetect_chain*. The resulting list of sources was inspected visually to remove possible spurious detections and cross-correlated with optical, infrared, and radio catalogs to search for possible identifications.

The properties of the most interesting sources (i.e., the brightest ones and those with a plausible identification) are reported in Table 1 and are shown in Figure 7. The EPIC-pn count rates and fluxes refer to the 0.5–2 keV range. The flux values marked with an asterisk were obtained from spectral analysis, while the remaining ones were derived assuming a power-law model with photon index $\Gamma = 1.7$ and a column density $N_{\rm H}^{\rm LOC} = 9.4 \times 10^{20}$ cm^{-2} (HI4PI Collaboration et al. 2016). The X-ray to optical flux ratio has been computed as

$$\log(f_{\rm X}/f_{\rm opt}) = \log f_{\rm X} + \frac{m}{2.5} + 5.37, \qquad \text{(A1)}$$

where $f_{\rm X}$ is the flux in the 0.5–12 keV range and m is magnitude in the red band. When no optical counterpart was present in the error region, a limiting magnitude $m = 21$ was assumed.

Eight sources are identified with foreground stars on the basis of their $f_{\rm X}/f_{\rm opt}$ and positional coincidence with objects of the GAIA and USNO-B1.0 catalogs. Several sources have been classified as quasars based on cross-correlation with catalogs of QSO candidates (Guo et al. 2018; Liao et al. 2019).

Table 1
The Brightest or Classified Detected Sources with X-Ray and Optical Parameters

Source Number	R.A. *	Decl.	Error (arcsec)	Rate (10^{-3} counts s^{-1})	Flux (10^{-14} erg cm^{-2} s^{-1})	Class	Rmag (mag)	$\log_{10}(X/O)$	Counterpart Name
1	04:05:10.43	−75:15:21.14	0.3	25.80 ± 1.38	$3.54^{+0.32*}_{-0.35}$	QSO	18.8	0.14 ± 0.02	USNO-B1.0 0147-0023343
2	04:04:42.37	−75:33:28.00	0.4	14.31 ± 1.13	$2.18^{+0.28*}_{-0.33}$	Unc.	20.5	0.61 ± 0.03	USNO-B1.0 0144-0021053
3	04:03:46.24	−75:32:37.90	2.2	9.59 ± 1.32	1.99 ± 0.27	Unc.	...	>0.59	... ...
4	04:03:12.50	−75:26:13.62	0.4	9.41 ± 0.63	1.96 ± 0.13	star	14.2	-2.33 ± 0.04	Gaia DR3 4628749515476145792
5	04:06:27.49	−75:26:19.46	0.7	11.24 ± 1.14	$1.78^{+0.27*}_{-0.31}$	Unc.	19.6	0.21 ± 0.04	USNO-B1.0 0145-0021710
6	04:06:12.80	−75:17:58.48	0.6	7.19 ± 0.88	1.49 ± 0.18	QSO	18.9	-0.39 ± 0.06	USNO-B1.0 0147-0023428
7	04:00:27.96	−75:23:53.16	0.6	6.82 ± 0.74	1.42 ± 0.15	Unc.	19.3	-0.32 ± 0.06	USNO-B1.0 0146-0022065
8	04:02:56.71	−75:26:55.67	0.4	8.53 ± 0.61	$1.25^{+0.14*}_{-0.16}$	Unc.	20.7	0.31 ± 0.04	USNO-B1.0 0145-0021402
9	04:00:21.17	−75:27:13.32	0.9	5.77 ± 0.92	1.20 ± 0.19	star	15.7	-1.88 ± 0.09	Gaia DR3 4628795798043612800
10	04:02:20.38	−75:23:27.74	0.5	5.69 ± 0.50	1.18 ± 0.10	Unc.	...	>0.32	... ...
11	04:03:56.23	−75:21:25.54	0.4	8.10 ± 0.59	$1.15^{+0.15*}_{-0.17}$	QSO	19.5	-0.18 ± 0.03	USNO-B1.0 0146-0022388
12	04:03:24.89	−75:10:54.67	0.9	5.09 ± 0.72	1.06 ± 0.15	Unc.	19.2	-0.45 ± 0.07	USNO-B1.0 0148-0024169
13	04:04:08.92	−75:22:26.51	0.6	4.85 ± 1.19	1.01 ± 0.25	Unc.	...	>0.22	... ...
14	04:01:34.12	−75:13:57.52	0.6	4.80 ± 0.65	1.00 ± 0.13	Unc.	20.1	-0.06 ± 0.06	Gaia DR3 4628825240041806080
15	04:04:23.92	−75:24:10.33	0.5	6.52 ± 0.56	$0.98^{+0.15*}_{-0.17}$	QSO	19.9	-0.10 ± 0.04	Gaia DR3 4628772532202907008
16	04:03:17.55	−75:15:42.63	0.7	4.33 ± 0.54	0.90 ± 0.11	Unc.	20.5	-0.05 ± 0.06	Gaia DR3 4628821460470380928
17	04:02:16.49	−75:21:34.49	0.5	4.23 ± 0.45	0.88 ± 0.09	Unc.	...	>0.10	... ...
18	04:01:26.12	−75:12:38.80	0.5	5.87 ± 0.78	$0.88^{+0.19*}_{-0.24}$	QSO	19.2	-0.27 ± 0.06	Gaia DR3 4628825313058849024
19	04:03:23.21	−75:28:12.74	0.6	6.25 ± 0.80	$0.84^{+0.14*}_{-0.17}$	Unc.	19.7	-0.19 ± 0.06	USNO-B1.0 0145-0021446
20	04:05:44.22	−75:29:58.64	0.9	3.98 ± 0.72	0.83 ± 0.15	QSO	18.2	-0.91 ± 0.08	Gaia DR3 4628768099796605056
21	04:00:45.39	−75:17:11.12	0.9	3.66 ± 0.68	0.76 ± 0.14	Unc.	...	>0.11	... ...
22	04:05:49.51	−75:19:17.97	1.1	3.58 ± 0.60	0.74 ± 0.12	star	11.0	-3.94 ± 0.09	Gaia DR3 4628771776288001536
23	04:03:55.22	−75:24:14.16	0.5	5.45 ± 0.50	$0.73^{+0.12*}_{-0.14}$	Unc.	20.5	0.01 ± 0.04	USNO-B1.0 0145-0021502
24	04:02:58.65	−75:33:57.98	1.6	3.41 ± 0.64	0.71 ± 0.13	star	10.4	-4.56 ± 0.19	Gaia DR3 4628746251297682816
25	04:03:34.46	−75:28:32.39	0.6	3.35 ± 0.43	0.70 ± 0.09	Unc.	...	>0.08	... ...
26	04:03:39.39	−75:26:05.71	0.7	3.24 ± 0.80	0.67 ± 0.17	Unc.	...	> -0.32	... ...
27	04:04:33.81	−75:26:58.40	0.8	3.23 ± 0.43	0.67 ± 0.09	Unc.	...	>0.07	... ...
28	04:01:49.74	−75:26:22.71	0.8	3.20 ± 0.43	0.66 ± 0.09	QSO	20.2	-0.23 ± 0.06	Gaia DR3 4628795179565576832
29	04:03:13.81	−75:31:45.63	1.1	3.19 ± 0.51	0.66 ± 0.11	Unc.	...	>0.04	... ...
30	04:03:18.83	−75:31:14.98	1.1	3.14 ± 0.58	0.65 ± 0.12	Unc.	...	>0.17	... ...
31	04:02:09.33	−75:28:11.85	1.2	3.06 ± 1.20	0.64 ± 0.25	Unc.	...	>0.13	... ...
32	04:02:49.05	−75:24:19.52	0.5	4.38 ± 0.43	$0.63^{+0.10*}_{-0.12}$	Unc.	...	>0.14	... ...
33	04:03:46.01	−75:27:59.01	0.8	2.98 ± 0.46	0.62 ± 0.10	star	15.9	-2.10 ± 0.08	USNO-B1.0 0145-0021480
34	04:00:42.97	−75:23:54.06	1.0	2.93 ± 0.52	0.61 ± 0.11	Unc.	...	> -0.01	... ...
35	04:01:35.81	−75:30:20.66	0.8	2.67 ± 0.50	0.55 ± 0.10	Unc.	...	>0.06	... ...
36	04:05:34.19	−75:23:39.68	1.0	2.55 ± 0.49	0.53 ± 0.10	Unc.	...	>0.02	... ...
37	04:02:22.90	−75:21:54.58	0.8	2.35 ± 0.69	0.49 ± 0.14	QSO	18.0	-1.49 ± 0.24	USNO-B1.0 0146-0022230
38	04:01:52.33	−75:32:03.49	1.6	2.26 ± 0.48	0.47 ± 0.10	Unc.	...	> -0.15	... ...
39	04:01:54.32	−75:21:17.31	0.8	2.16 ± 0.36	0.45 ± 0.07	Unc.	...	> -0.12	... ...
40	04:01:20.27	−75:14:59.55	1.3	2.15 ± 0.48	0.45 ± 0.10	Unc.	19.8	-0.58 ± 0.12	USNO-B1.0 0147-0022964
41	04:00:17.79	−75:23:58.63	1.9	2.11 ± 0.50	0.44 ± 0.10	star	12.3	-3.67 ± 0.13	Gaia DR3 4628796038561772928
42	04:03:35.41	−75:18:00.50	0.8	2.10 ± 0.35	0.44 ± 0.07	Unc.	...	> -0.32	... ...
43	04:06:10.78	−75:21:28.39	0.9	2.08 ± 0.63	0.43 ± 0.13	QSO	20.1	-0.41 ± 0.13	USNO-B1.0 0146-0022585
44	04:04:14.29	−75:19:28.19	1.0	2.08 ± 0.59	0.43 ± 0.12	Unc.	...	> -0.25	... ...
45	04:05:43.35	−75:25:55.43	1.5	1.92 ± 0.47	0.40 ± 0.10	Unc.	...	> -0.23	... ...
46	04:03:21.87	−75:24:59.60	0.9	1.92 ± 0.32	0.40 ± 0.07	Unc.	...	> -0.31	... ...
47	04:02:49.10	−75:28:45.49	1.1	1.88 ± 0.34	0.39 ± 0.07	Unc.	...	> -00.19	... ...
48	04:04:01.56	−75:27:03.37	0.8	1.75 ± 0.33	0.36 ± 0.07	Unc.	...	> -0.29	... ...
49	04:04:27.08	−75:32:50.58	1.0	1.74 ± 0.46	0.36 ± 0.10	QSO	20.0	-0.63 ± 0.15	Gaia DR3 4628745014347539968
50	04:03:48.28	−75:25:31.90	0.9	1.62 ± 0.34	0.34 ± 0.07	Unc.	...	> -0.28	... ...
51	04:03:07.43	−75:27:48.46	1.0	1.43 ± 0.31	0.30 ± 0.06	Unc.	...	> -0.50	... ...
52	04:04:13.72	−75:25:15.45	1.4	1.23 ± 0.29	0.26 ± 0.06	star	18.5	-1.46 ± 0.12	USNO-B1.0 0145-0021522
53	04:04:02.71	−75:17:25.46	1.2	1.05 ± 0.29	0.22 ± 0.06	star	19.5	-1.05 ± 0.13	USNO-B1.0 0147-0023232

Note.
* flux value from spectral fit.

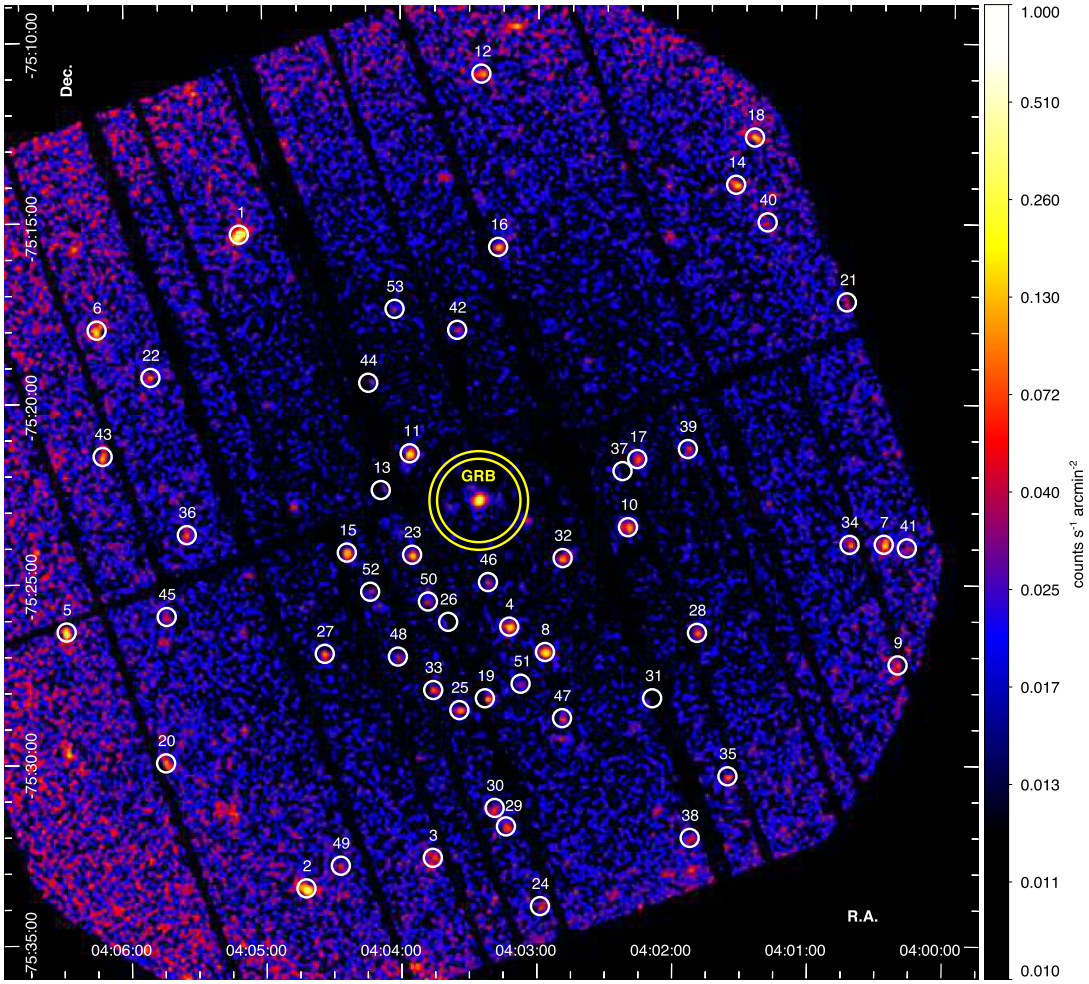

Figure 7. EPIC-pn image in the 0.3–10 keV energy range of the field of GRB 230307A. The yellow circles show the expected position of scattering rings produced by dust in the Magellanic Bridge, for distances of 50 kpc (outermost circle) and 70 kpc (innermost circle). The sources listed in Table 1 are indicated by the small circles.

ORCID iDs

Sandro Mereghetti https://orcid.org/0000-0003-3259-7801
Michela Rigoselli https://orcid.org/0000-0001-6641-5450
Ruben Salvaterra https://orcid.org/0000-0002-9393-8078
Andrea Tiengo https://orcid.org/0000-0002-6038-1090
Dominik P. Pacholski https://orcid.org/0009-0001-3911-9266

References

Abbott, B. P., Abbott, R., Abbott, T. D., et al. 2017a, ApJL, 848, L12
Abbott, B. P., Abbott, R., Abbott, T. D., et al. 2017b, ApJL, 848, L13
Ahumada, T., Singer, L. P., Anand, S., et al. 2021, NatAs, 5, 917
Antonelli, L. A., D'Avanzo, P., Perna, R., et al. 2009, A&A, 507, L45
Arnaud, K. A. 1996, in ASP Conf. Ser. 101, Astronomical Data Analysis Software and Systems V, ed. G. H. Jacoby & J. Barnes (San Francisco, CA: ASP), 17
Burns, E., Goldstein, A., Lesage, S., Dalessi, S. & Fermi-GBM Team 2023a, GCN, 33414, 1
Burns, E., Svinkin, D., Fenimore, E., et al. 2023b, ApJL, 946, L31
Burrows, D. N., Gropp, J. D., Osborne, J. P., et al. 2023, GCN, 33465, 1
Campana, S., Lazzati, D., Perna, R., Grazia Bernardini, M., & Nava, L. 2021, A&A, 649, A135
Campana, S., Lazzati, D., Ripamonti, E., et al. 2007, ApJL, 654, L17
Chen, B. Q., Guo, H. L., Gao, J., et al. 2022, MNRAS, 511, 1317
Dalessi, S. & Fermi GBM Team 2023, GCN, 33407, 1
Dalessi, S., Roberts, O. J., Meegan, C. & Fermi GBM Team 2023, GCN, 33411, 1
Dichiara, S., Tsang, D., Troja, E., et al. 2023, ApJL, 954, L29
Draine, B. T. 2003, ApJ, 598, 1026
Frederiks, D., Svinkin, D., Lysenko, A. L., et al. 2023, ApJL, 949, L7
Fynbo, J. P. U., Watson, D., Thöne, C. C., et al. 2006, Natur, 444, 1047
Gabriel, C., Denby, M., Fyfe, D. J., et al. 2004, in ASP Conf. Ser. 314, Astronomical Data Analysis Software and Systems (ADASS) XIII, ed. F. Ochsenbein, M. G. Allen, & D. Egret (San Francisco, CA: ASP), 759
Gaia Collaboration, Luri, X., Chemin, L., et al. 2021, A&A, 649, A7
Galama, T. J., Vreeswijk, P. M., van Paradijs, J., et al. 1998, Natur, 395, 670
Goldstein, A., Veres, P., Burns, E., et al. 2017, ApJL, 848, L14
Green, G. 2018, JOSS, 3, 695
Grupe, D., Gronwall, C., Wang, X.-Y., et al. 2007, ApJ, 662, 443
Guo, S., Qi, Z., Liao, S., et al. 2018, A&A, 618, A144
HI4PI Collaboration, Ben Bekhti, N., Flöer, L., et al. 2016, A&A, 594, A116
Hjorth, J., Sollerman, J., Møller, P., et al. 2003, Natur, 423, 847
Jacyszyn-Dobrzeniecka, A. M., Skowron, D. M., Mróz, P., et al. 2016, AcA, 66, 149
Kouveliotou, C., Meegan, C. A., Fishman, G. J., et al. 1993, ApJL, 413, L101
Lallement, R., Vergely, J. L., Babusiaux, C., & Cox, N. L. J. 2022, A&A, 661, A147
Lazzati, D., & Perna, R. 2002, MNRAS, 330, 383
Levan, A., Gompertz, B. P., Salafia, O. S., et al. 2023a, arXiv:2307.02098
Levan, A. J., Watson, D., Hjorth, J., et al. 2023b, GCN, 33580, 1
Liao, S.-L., Qi, Z.-X., Guo, S.-F., & Cao, Z.-H. 2019, RAA, 19, 029
Mochkovitch, R., Hernanz, M., Isern, J., & Martin, X. 1993, Natur, 361, 236
Nakar, E. 2007, PhR, 442, 166
Narayan, R., Paczynski, B., & Piran, T. 1992, ApJL, 395, L83
Nasa High Energy Astrophysics Science Archive Research Center (Heasarc) 2014, HEAsoft: Unified Release of FTOOLS and XANADU, Astrophysics Source Code Library, ascl:1408.004
Nicuesa Guelbenzu, A., Klose, S., Rossi, A., et al. 2011, A&A, 531, L6

Norris, J. P., Cline, T. L., Desai, U. D., & Teegarden, B. J. 1984, Natur, 308, 434
Perna, R., & Lazzati, D. 2002, ApJ, 580, 261
Perna, R., & Loeb, A. 1998, ApJ, 501, 467
Pintore, F., Tiengo, A., Mereghetti, S., et al. 2017, MNRAS, 472, 1465
Rastinejad, J. C., Gompertz, B. P., Levan, A. J., et al. 2022, Natur, 612, 223
Rossi, A., Rothberg, B., Palazzi, E., et al. 2022, ApJ, 932, 1
Rouco Escorial, A., Gompertz, B., Fong, W., et al. 2023, GCN, 33558, 1
Savchenko, V., Bazzano, A., Bozzo, E., et al. 2017a, A&A, 603, A46
Savchenko, V., Ferrigno, C., Kuulkers, E., et al. 2017b, ApJL, 848, L15
Smith, R. K., Dame, T. M., Costantini, E., & Predehl, P. 2006, ApJ, 648, 452
Smith, R. K., Valencic, L. A., & Corrales, L. 2016, ApJ, 818, 143
Stanek, K. Z., Matheson, T., Garnavich, P. M., et al. 2003, ApJL, 591, L17
Starling, R. L. C., Vreeswijk, P. M., Ellison, S. L., et al. 2005, A&A, 442, L21
Strüder, L., Briel, U., Dennerl, K., et al. 2001, A&A, 365, L18
Sun, H., Wang, C. W., Yang, J., et al. 2023, arXiv:2307.05689
Svinkin, D., Frederiks, D., Ulanov, M., et al. 2023, GCN, 33427, 1
Tiengo, A., & Mereghetti, S. 2006, A&A, 449, 203
Tiengo, A., Pintore, F., Vaia, B., et al. 2023, ApJL, 946, L30
Tiengo, A., Vianello, G., Esposito, P., et al. 2010, ApJ, 710, 227
Troja, E., Fryer, C. L., O'Connor, B., et al. 2022, Natur, 612, 228
Turner, M. J. L., Abbey, A., Arnaud, M., et al. 2001, A&A, 365, L27
Valan, V., Larsson, J., & Ahlgren, B. 2023, ApJ, 944, 73
Vaughan, S., Willingale, R., O'Brien, P. T., et al. 2004, ApJL, 603, L5
Vaughan, S., Willingale, R., Romano, P., et al. 2006, ApJ, 639, 323
Vianello, G., Götz, D., & Mereghetti, S. 2009, A&A, 495, 1005
Vianello, G., Tiengo, A., & Mereghetti, S. 2007, A&A, 473, 423
Viganò, D., & Mereghetti, S. 2009, in Proc. The Extreme Sky: Sampling the Universe above 10 keV Vol. 096 (Trieste: SISSA), 49
von Kienlin, A., Beckmann, V., Rau, A., et al. 2003, A&A, 411, L299
Wang, Y., Xia, Z.-Q., Zheng, T.-C., Ren, J., & Fan, Y.-Z. 2023, ApJL, 953, L8
Watson, D., Vaughan, S. A., Willingale, R., et al. 2006, ApJ, 636, 967
Wiersema, K., van der Horst, A. J., Kann, D. A., et al. 2008, A&A, 481, 319
Wilms, J., Allen, A., & McCray, R. 2000, ApJ, 542, 914
Xiong, S., Wang, C., Huang, Y. & Gecam Team 2023, GCN, 33406, 1
Yang, B., Jin, Z.-P., Li, X., et al. 2015, NatCo, 6, 7323
Yang, J., Ai, S., Zhang, B.-B., et al. 2022, Natur, 612, 232
Yang, Y.-H., Troja, E., O'Connor, B., et al. 2023, arXiv:2308.00638
Zhang, B. 2006, Natur, 444, 1010
Zubko, V., Dwek, E., & Arendt, R. G. 2004, ApJS, 152, 211